
Article:
Zhang, H., Wu, J., Robert, C. orcid.org/0000-0001-5035-6134 et al. (2 more authors) (2022) 3D printing and epoxy-infusion treatment of curved continuous carbon fibre reinforced dual-polymer composites. Composites Part B: Engineering, 234. 109687. ISSN 1359-8368

https://doi.org/10.1016/j.compositesb.2022.109687

3D printing and epoxy-infusion treatment of curved continuous carbon fibre reinforced dual-polymer composites

Haoqi Zhang, Jiang Wu, Colin Robert, Conchúr M. Ó Brádaigh, Dongmin Yang*

School of Engineering, Institute for Materials and Processes, University of Edinburgh, EH9 3FB, Edinburgh, UK

Abstract

A manufacturing technique was developed to fabricate curved continuous carbon fibre reinforced composites based on 3D printing and epoxy-infusion treatment. Composite preforms were first manufactured by material-extrusion based 3D printing of continuous carbon fibre reinforced thermoplastic polyamide-6 (PA-6) filaments. Powder thermoset epoxy was added to the preforms to fill up the gaps, remove air voids and enhance the interfacial bonding through a traditional vacuum bagging and oven curing process. Uniaxial tensile tests showed that the stiffness and strength of the printed composites were increased by 29.3% and 22.1%, respectively, compared to the thermoplastic-only composite specimens. The epoxy-infusion treatment technique was also adopted to manufacture composites with curved fibre alignment and investigate the performance of 3D printed notched specimens under uniaxial tension. It was shown that the placement of continuous carbon fibres along the principal stress trajectories increased the failure strength and the fracture toughness of the composites by 81% and 157% respectively, compared to the unidirectional and concentric placement methods.

Keywords: Material-extrusion based 3D printing; epoxy-infusion treatment; dual-polymer composites; principal stress trajectory; curved continuous carbon fibre.

* Corresponding author. Email: Dongmin.Yang@ed.ac.uk

1. Introduction

3D printing of composites has seen fast development in the past decades, as it offers the benefits of manufacturing complex composite products at low cost for fixtures, tools, moulds as well as load-bearing structures [1, 2]. One of the most attractive printing techniques is the material-extrusion based printing of continuous carbon fibre reinforced thermoplastic (cCFRTP) composites, where the filament is melted and deposited layer by layer to form a 3D composite part [3, 4]. As the printing path can be steered during the printing process, material-extrusion based printing has the potential to manufacture highly complex composite structures without additional cutting or drilling [5], which can lead to better performance compared with conventional manufacturing techniques [6, 7].

One of the most challenging issues for material-extrusion based 3D printing of cCFRTP composites, however, is the inadequate impregnation of the fibres by the polymer matrix [8, 9] and the resulting substantial air voids [10], mainly due to the high viscosity of the thermoplastic. Another problem, the insufficient inter-diffusion between two adjacent layers [11], is usually aggravated due to the low fluidity of the matrix when mixed with continuous fibres. This results in the printed composites having less competitive mechanical properties (strength and stiffness) than traditionally manufactured cCFRTP, and can also cause premature failure and delamination during their loading process [12]. For example, the commercial 3D printer Mark Two from Markforged® is capable of printing continuous CF/PA6 filament, but the uniaxial tensile strength of the printed composites is 30% lower than traditionally manufactured cCFRTP with the same polymer matrix and fibre volume fraction [13, 14]. Post-printing techniques have been reported to compact the printed composites and thus improve their mechanical properties, *e.g*. hot-press [15, 16]. Other in-situ consolidation techniques have also been reported, *e.g*. micro-screw [11], microwave enhanced consolidation [17], roller compaction [18], *etc*. In addition, lots of researches have also been carried out to optimise the

printing paths in order to maximise the reinforcement of the continuous carbon fibres. For example, placement of fibres along principal stress trajectories [19-21] and optimisation of the fibre orientation together with optimisation of the structural topology [22-24] have been demonstrated.

When the curved fibre paths are customised, there are gaps between the printing paths at some locations [25]. Therefore, an infill technique needs to be adopted to bridge the gaps, reduce the porosity and ensure the structural integrity of the printed composites. However, the aforementioned in-situ consolidation techniques could not reduce the porosity to below 1%. For example, there was still a porosity of 5.7% for carbon fibre reinforcements under low-pressure printing [26]. Also, the compaction roller caused an irregular side surface due to the hatch spacing, and then increased voids in the vicinity of the side edges (with porosity of 3%) [27]. The processes promising better impregnation between fibre and matrix could not eliminate the gaps between the print paths [18]. As an alternative, the traditional hot-press technique is also less attractive due to the cost of heated matched-metal tooling required. Although the porosity can be decreased by less than 1% with temperatures of up to 250 °C, the original polymer matrix surrounding the continuous fibres was melted, and thus the customised fibre placement could not be maintained anymore [28]. Apparently, it would be of very limited use to manufacture 3D printed composites without considering the customisation of the anisotropic properties [7].

In this study, we present a low-cost post-processing technique to address this issue. A low viscosity powder epoxy is used to fill up the gaps and to enhance the composite properties after consolidation by vacuum bagging only and oven curing. More importantly, the customised fibre alignment is maintained during the post-processing step, because of the lower melt and curing temperature [29] of the powder epoxy. This manufacturing technique can be used for certain cases with complex geometries and further expands the use of the mechanism of curved

fibre placement.

This paper is organised as follows. Section 2 introduces the manufacturing processes of 3D printing of CF/PA-6 preforms and the post-processing with powder epoxy. Section 3 presents the set-up of uniaxial tensile tests and the design of cases, including the UD 0˚ samples and the single-edge notched samples. The result and discussion section first compares the mechanical performance of the UD 0˚ samples before and after the post-processing. Characterisation of the cross-sections and fracture profiles is carried out via scanning electron microscopy (SEM). The experimental test results for single-edge notched plates are then shown, including the strength, fracture toughness and strain distribution obtained from the digital image correlation (DIC), in order to demonstrate the fabrication with curved fibre alignment and evaluate the improvement.

2. 3D printing and epoxy-infusion treatment

2.1 3D printing of CF/PA-6 preforms

A Prusa i3 MK3s printer was used in this study and the schematic diagram of 3D printing CF/PA-6 composite preforms is shown in Figure 1(a). The printing material, 0.375mm-diameter 1K carbon fibre (CF) filament, was sourced from Markforged® (Massachusetts, USA). Previous authors had evidenced that polyamide 6-I (PA6-I) was the polymer matrix for CF filaments and the polymer coating was a polyamide 6 (PA6) [30]. The cross-section of the filament is shown in Figure 1(b), in which noticeable air bubbles and weak fibre/matrix bonding were observed. In the material-extrusion based 3D printing process, the CF filaments were heated to the temperature of 245°C and the off-distance between the nozzle tip and the print bed was set to 0.125 mm, as recommended by the Markforged®. The print bed was not heated during the printing process (kept at room temperature = 20-25°C), because the warpage problem would not occur as in the printing of pure thermoplastic, due to the reinforcement of continuous fibres. Moreover, quick cooling is needed in order to ensure the bonding between the printed filament and the bed. A brass nozzle with an inner diameter of 1.2 mm was used

[31] and the speed of nozzle movement was consistent with the 10mm/s feed rate of the filament, which means the free end of the CF filament is slightly under tension due to the twine of the spool, but the feeding of filament is not affected. Samples were printed onto an unheated Garolite print plate which was coated in a layer of PVA, to ensure adequate adhesion during printing. Since the filaments used in this study contain continuous fibres and the toolpath cannot be started and stopped during the printing, the continuous toolpath (G-code) was necessary. It was generated via MATLAB and then transferred to the printer. The generation of continuous G-code will be presented in detail, together with the design of curved fibre placement in the following section.

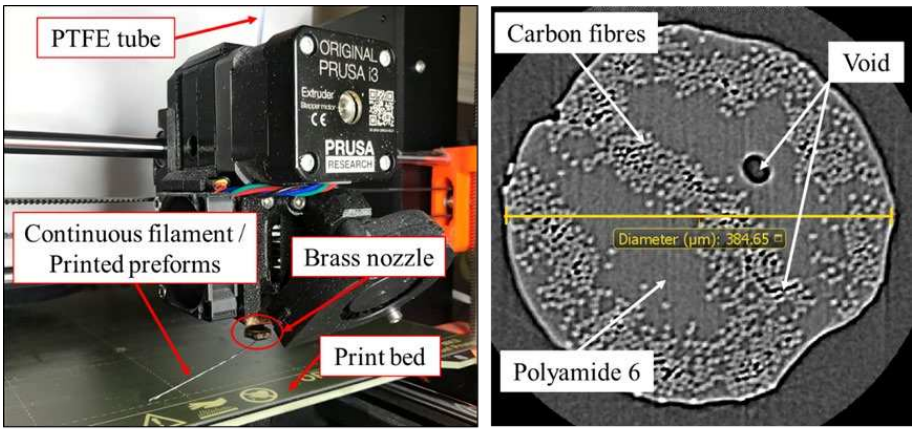

Figure 1. (a) Schematic diagram for 3D printing of composites CF/PA-6 preforms (b) the cross-section of the CF filament

2.2 Post-processing of thermoplastic-thermosetting dual matrix composites

The thermosetting epoxy powder (PE6405, density 1.22 g/cm3) has been engineered by Swiss CMT (Siebnen, Switzerland) and then produced by FreiLacke (Bräunlingen, Germany). As shown by Differential Scanning Calorimetry (DSC) characterisation in Figure 2(a), the epoxy sinters and melts at around 45-60 °C. The low melt viscosity (minimum of 1.26 Pa·s at 120°C) and low rate of cure below 120 °C allow more time to fully infuse the CF/PA-6 preforms [29]. Then the curing is carried out through a heat-activated catalytic process, where the curing agent requires a temperature of at least 150 °C for reaction initiation [32, 33].

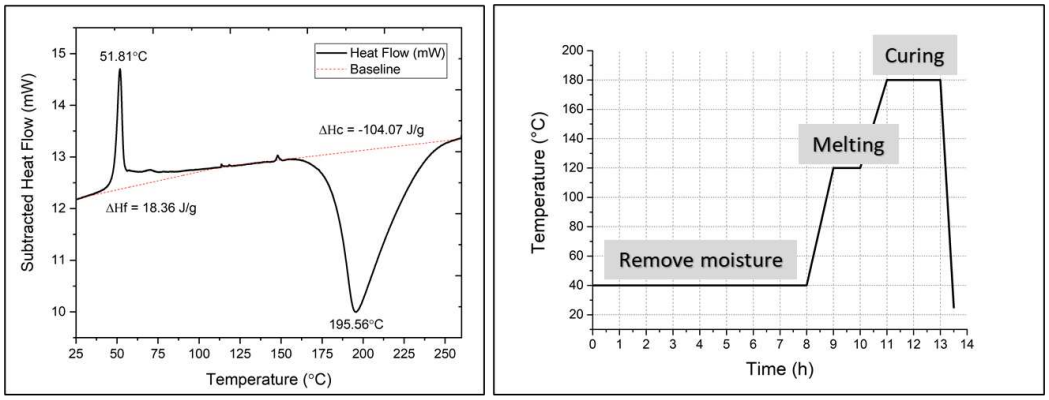

(a) (b)

Figure 2. (a) DSC characterisation of the PE6405 epoxy powder [29] (b) the heat cycling of the post-processing

As shown in Figure 3(a), the aluminium-made plate with a polytetrafluoroethylene (PTFE) non-stick ply was used as the bottom mould. The powder-epoxy was sprinkled manually, only on top of the printed CF/PA-6 preforms, allowing to fill the voids due to a very low viscosity [32] since the preforms in our study were thin. For the samples with the larger thickness (that were composed of more than two CF/PA-6 preforms), the powder was sprinkled between the preforms to enhance the adhesion. The peel ply and breather fabric allowed to remove melted powder epoxy excess. As shown in Figure 3(b), the 3D printed CF/PA-6 preforms with sprinkled powders were vacuum-bagged and then put into an oven for heating. Based on the thermal property in Figure 2(a) and the melting/curing temperature gap of PE6405 epoxy, a three-stage heating profile was used, as presented in Figure 2(b). The pre-curing cycle with vacuum bagging was firstly set at 40 °C (lower than the melting temperature) for 8 hours to remove all possible moisture from the powder. The temperature was then ramped to 120 °C for 1 hour, melting the powder without any curing. During this stage, the low viscosity of the melted epoxy would enable adequate impregnation to infill the gaps/voids of the CF/PA-6 preforms. Following this, the specimen was cured at 180 °C for 2 hours in order to completely consolidate the epoxy. It was noted that the pre-heating time could be shortened or even eliminated if the powder-epoxy was properly stored. Also, the duration for melting/curing can

be reduced based on the power of the heat source and the dimension of the specimens.

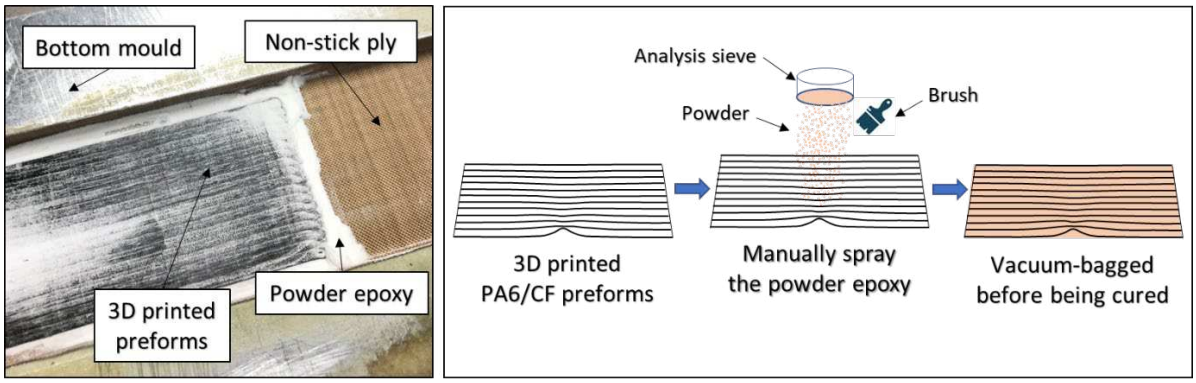

Figure 3. (a) Bottom mould and printed CF/PA-6 preforms with sprinkled powders (b) the schematic diagram of the post-processing treatment

3. Mechanical testing

3.1 Instruments and 2D-DIC set-up

The mechanical tests were performed using an MTS Criterion® Model 45 (C45.305) with a 300 kN load cell. A crosshead speed of 0.5 mm/min was used for all tests and the samples were clamped in hydraulic grips with a clamping pressure of approx. 80 bar. In each type of test, three specimens were tested. A speckle pattern was applied to the surface of each specimen for the digital image correlation (DIC). All the data obtained from the 2D video extensometer were processed through a MATLAB script to measure full-field displacement and strains [34].

3.2 Uniaxial tensile tests

The uniaxial tensile tests of the Unidirectional (UD) 0˚ samples were carried out according to ASTM D3039 (Standard Test Method for Tensile Properties of Polymer Matrix Composite) to study the tensile strength and stiffness of samples before and after post-processing. The length, width and thickness of the samples were 200mm, 15mm and 1mm, respectively. The test specimens were end tabbed with ±45° GRFP (length of 50mm) and VTFA400 adhesive film sourced from SHD Composites Ltd, which acts to minimise strain concentrations at the gripping points. Since the thickness of the printing layer is 0.15mm approximately, eight layers

with 0° unidirectional fibres were printed for each sample. The tensile strength and stiffness will be calculated based on the measured dimensions of each sample.

As per ASTM E1922-04 (standard test method for translaminar fracture toughness of laminated and pultruded polymer matrix composite materials), the uniaxial tensile tests of single-edge notched plates were also conducted as another case study, in order to demonstrate the fabrication of composites with low-porosity and customised curved fibre alignment. Similar tests to this standard were carried out in previous research about composites [35-37]. The performance of optimised fibre placement along principal stress trajectories, including the strength and fracture toughness, was investigated and compared with the unidirectional and concentric placement methods. The dimensions of the single-edge notched samples are 200mm-length, 36mm-width and 1mm-thickness. A single-edge notch is designed in the horizontal centreline of the plate with the 4mm-length and 4mm-width and three different fibre filling patterns were adopted. For the unidirectional placement in Figure 4(a), the 4×4 mm notch would be mechanically cut by a wet saw, which is a traditional method for manufacturing composites with geometric singularity. Concentric placement (Figure 4b) is the most popular method for the material-extrusion based 3D printing of thermoplastic materials, in order to achieve a better surface and a dense infill for 3D printed composites with complex geometries. It was also used in the Eiger system for Markforged's 3D printers for continuous fibres [38]. For the optimised placement method (in Figure 4c), the principal stress trajectories were generated from finite element analysis (FEA) of a neat polymer matrix based on the tensile loading condition and used as the guidance for the path design of continuous carbon fibres. This optimised placement method with customised curved fibre paths aims to achieve a better mechanical performance, as described in detail in our previous work [19]. In this placement method, the coordinates and angles for maximum/minimum principal stress of each element were imported into Tecplot 360 software, in which we set a consistent distance (1mm) of each

line at one side of the domain and then the software would generate the streamlines to the other side based on the orientation of each element. An area with denser fibre paths and slight overlap was created around the notch automatically, while a relatively sparse distribution appeared at the horizontal area far from the notch. This automatic response of the fibre placement method is to release the stress concentration around the geometric singularity and enhance the structure, which can also be seen in other research about stress-lines fibre placement method [20]. The stress trajectories were created by entering the start position, gap and number of streamlines. The end-to-end connection of these streamlines was achieved via MATLAB based on the principle of minimising the fibre usage and ensuring accurate fibre paths in the domain.

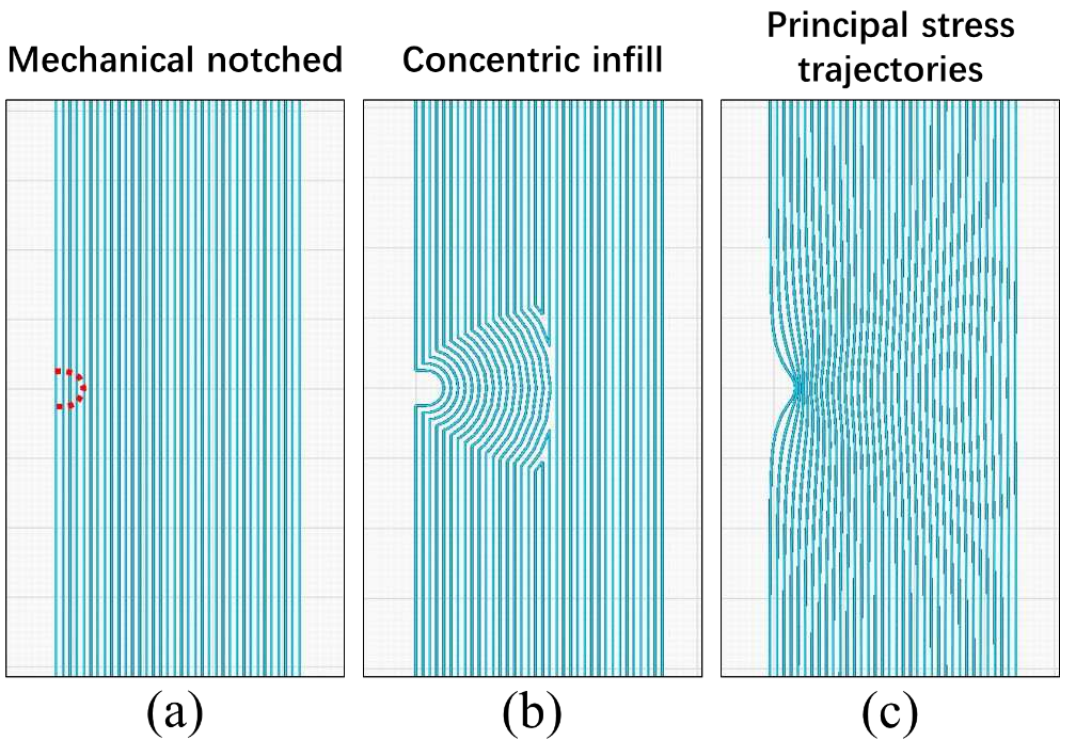

Figure 4. Fibre placement of three kinds of single-edge notched samples: (a) Mechanical notched (b) Concentric infill (c) Principal stress trajectories

4. Results and discussion

In this section, the thermal properties of dual-polymer composites are first presented. Then the SEM characterisation for the cross-section of UD 0˚ samples is presented to reveal the porosity and bonding condition before and after the post-processing. For the results of the mechanical

tests, the tensile properties and the fracture profiles of the standard UD 0˚ samples are first presented for comparison purposes (before and after post-processing). Then the notched samples after post-processing are demonstrated to discuss the effect of different fibre placement methods.

4.1 Material characterisation

4.1.1 Thermal and microstructure characterisation

The results of Dynamic Mechanical Analysis (DMA) for the CF/PA-6 printed preforms and the dual-polymer composites are shown in Figure 5. The dual cantilever mode was conducted using a PerkinElmer® DMA 8000, with the temperature ramp of 2 °C/min from 50 °C to 160 °C. For the CF/PA-6 printed preforms, the onset of the rubbery state was about 80 °C and reached its glass transition point T_g (first peak of the tan delta) at 102.3 °C. Then the material transited to the viscous state quickly, with the viscous flow temperature (second peak of the tan delta) of 128.0 °C. The uneven surface of samples after DMA (in Figure 5a) also indicated the plastic deformation of the material during the viscous state. This thermal-mechanical behaviour of CF/PA-6 preforms subsequently allowed for better consolidation and void removal during the melting phase of powder epoxy at 120 °C. After post-processing with epoxy, the glass transition temperature was improved to 128.7 °C and no viscous state was found. It indicated a better thermal-mechanical behaviour of the dual-polymer composites in this study and is assumed to be caused by the hardness of cured epoxy as well as the reaction between nylon-6 and epoxy. The main reaction is the nucleophilic attack on the oxirane ring by the amide nitrogen of the nylon [39], as shown in Figure 6a. It follows an alternate ring-opening copolymerization mechanism that leads to polyester and polyether networks [40], which is a typical reaction for the curing of epoxy resin with an amine hardener.

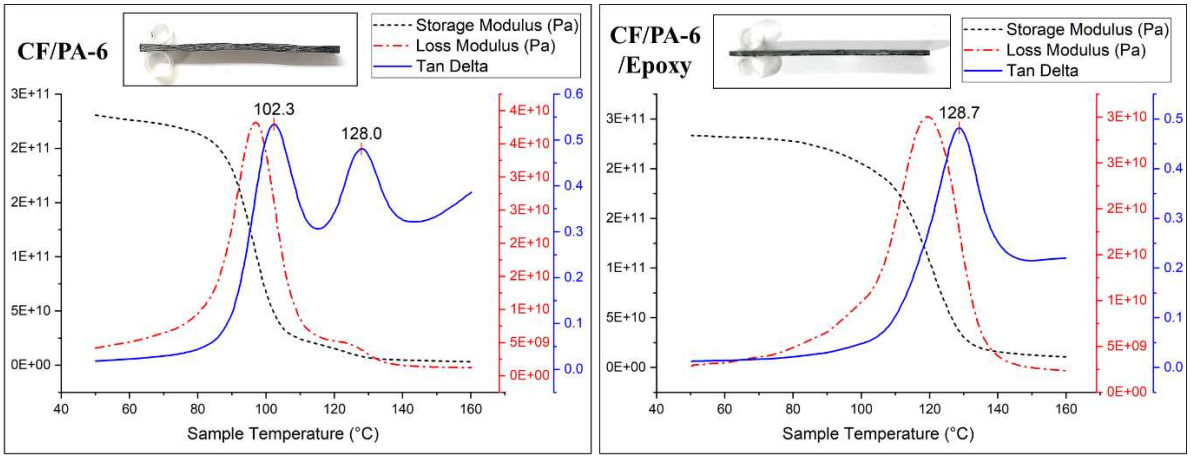

(a) (b)

Figure 5. DMA traces of (a) CF/PA-6 and (b) CF/PA-6/Epoxy.

The thermal properties were also evaluated using DSC, with the temperature ramp of 20 °C/min from 30 °C to 300 °C. T_g was only defined via DMA, however, since it is more sensitive to the glass transition point than DSC. As shown in Figure 6b, only one glass transition peak was observed for the CF/PA-6 preforms. The melting peak was found to be absent even when the samples were exposed to 300 °C. Previous authors have highlighted that the shape and size of the melting peaks observed in DSC are dependent on the thermal history of the nylon polymer [41]. Since the curing temperature used is lower than the melting point of PA6, the alignment of straight/curved continuous fibres can be generally maintained during the consolidation.

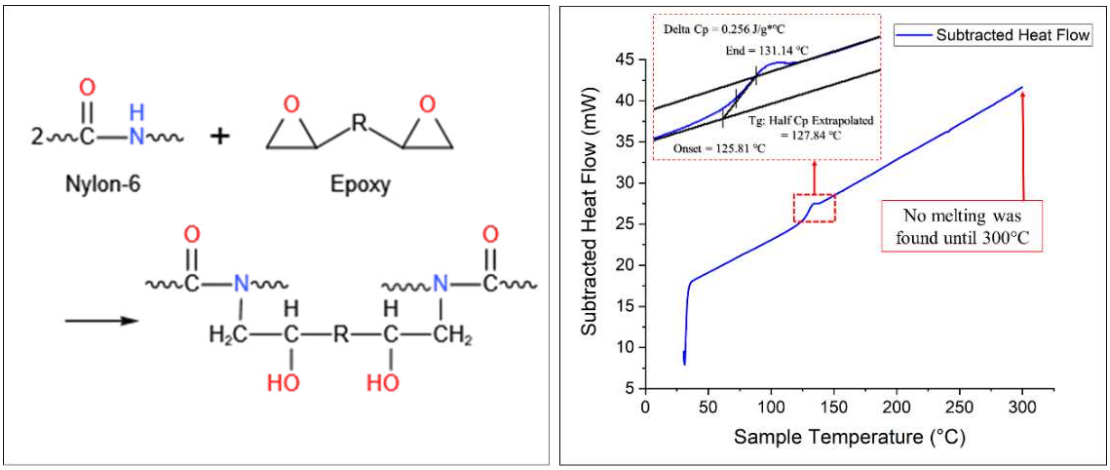

(a) (b)

Figure 6. (a) Reaction mechanism of PA-6/epoxy [39] (b) DSC characterisation of the 3D printed CF/PA-6 preforms.

A comparison of the cross-sections is shown in Figure 7. The UD 0˚ specimens (before testing) were cut into 5 pieces and embedded in epoxy. These samples were then polished using a Saphir® 520 polishing machine, with sandpaper from P400, P800 to P1200 grit and diamond polishing suspension from 9, 3 to 1 μm. The cross-sections were observed using a HITACHI® TM400 Tabletop Microscope. As shown in Figure 7a, two kinds of voids were observed in the 3D printed CF/PA-6 preforms, including the voids between layers and the gaps between the fibre paths. But no apparent voids can be found in the dual-polymer composites after the post-processing, also the melted epoxy can be observed to infiltrate to the composites from the gaps between the fibre paths, as shown in Figure 7b. The weight and dimensions before and after post-processing were measured, wherein the weight was increased by 4.88% after post-processing (thus the weight fraction of the infilled epoxy was 4.67%). The thickness of the samples was reduced by approximately 6%, which mainly resulted from the vacuum pressure acting on the top and the rubbery/viscous state of the PA-6 matrix (at the temperature of 120°C). A relatively consistent width was obtained before and after the post-processing, also with filleted corners of the sample, because the vacuum pressure limited the extension on both sides and the excessive melted epoxy would be absorbed by the breather fabric (due to its low viscosity).

Detailed SEM characterisations of the cross-section are shown in Figure 8 to further evaluate the microstructures, in which the observed position of the CF/PA-6 preforms located at the area without those large pores as shown in Figure 7a. And 15 pictures were taken for samples before and after post-processing respectively to measure the volume fraction of fibre and void. The calculation was performed on Avizo software with two filters to differentiate the matrix, fibres and void, in which the same thresholds were used for all the pictures. The fibre volume fraction before post-processing was measured as 31.7%. During the printing process, the porosity in the central part of the single printed strip decreased due to the compressive force from the tip of

the nozzle. On the contrary, the edges of the strip included more voids due to the uneven pressure, as mentioned in [31]. Before post-processing, the porosity of the single stripe and the whole cross-section were 2.69% and 8.46%, respectively. Also, matrix-rich areas and significant pores were found, as shown in Figure 8a. Besides that, apparent cracks were observed to propagate along with the interface between printing layers. It was assumed to be caused by the temperature difference between the printing layer and the printed layer below it during the printing process. Furthermore, an additional test was conducted for the sample processed only by the vacuum-bagging without epoxy powder (using the same heating cycling). As can be in Figure 8b, the volume of voids was reduced, because the softened PA-6 matrix was compressed in the process. However, some isolated pores, which possibly originated from the gaps between fibre paths, were still trapped in the sample due to the lack of infill material. On the contrary, almost no voids were found in the cross-section of the dual-polymer specimens and the inter-stripes gap was also eliminated, as shown in Figure 7b & 8c. The infill epoxy and the vacuum pressure slightly improved the fibre volume fraction to 34.6% and dramatically reduced the porosity to 0.06% (hard to be accurately measured due to the small volume). As the gaps between strips were filled up by the epoxy, the boundaries of the strips were not distinctive and only the porosity of the whole cross-section was measured. However, matrix-rich areas still existed since the matrix of CF/PA-6 filament stayed solid under the curing temperature. A few micro-cracks can be found but they were relatively small compared with those in the samples before post-processing. These may originate from the thermal stresses induced by the heterogeneous interface between thermoset and thermoplastic resin.

Table 1. Fibre and void volume fraction before and after post-processing

	Fibre volume fraction	Void volume fraction
Printed preforms before post-processing (CF/PA-6)	31.7%	2.69% (central area of the strips) 8.46% (whole cross-section)
Dual-polymer composites (CF/PA-6/Epoxy)	34.6%	0.06% (whole cross-section)

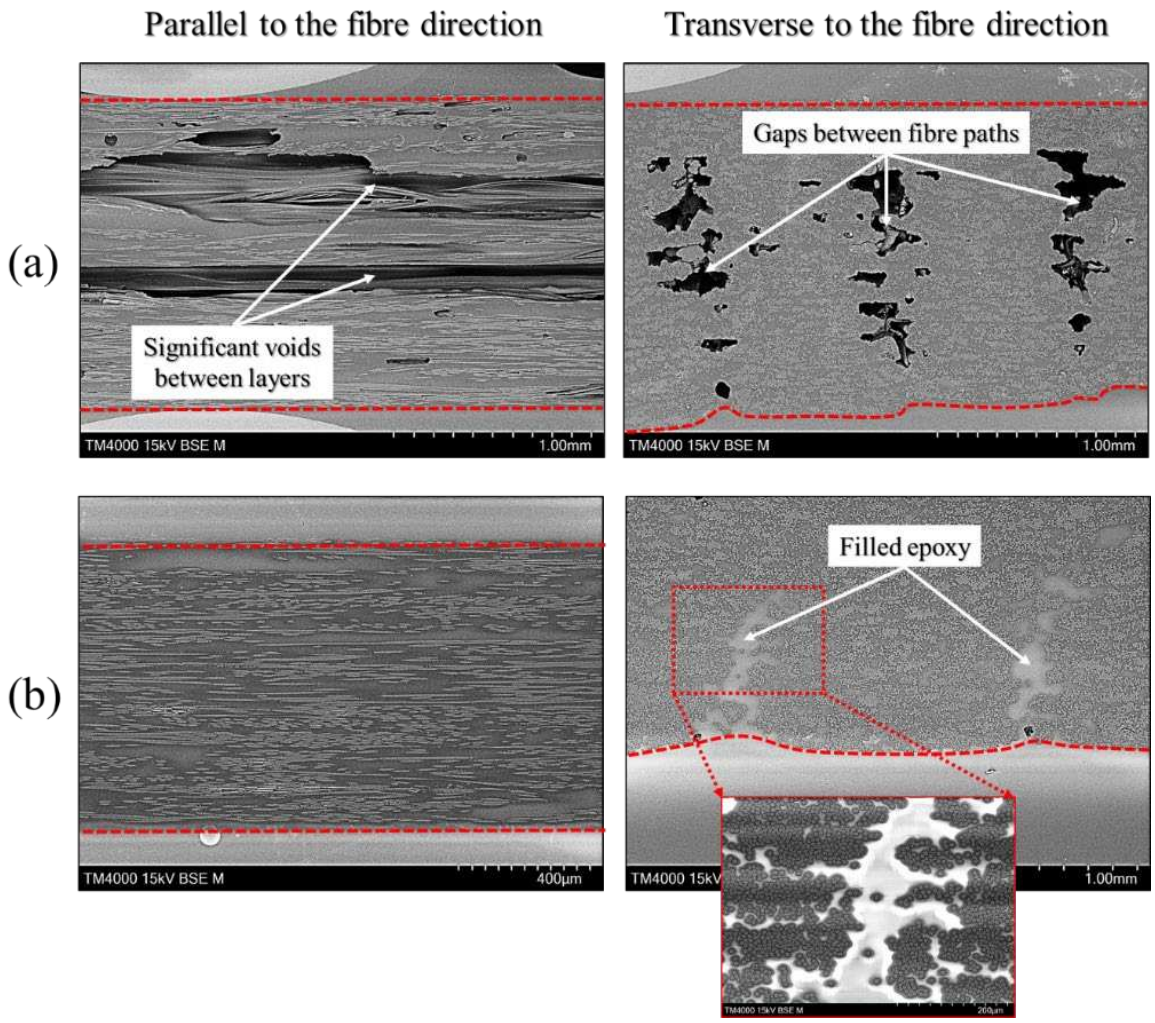

Figure 7. Comparison of the cross-sections: (a) 3D printed CF/PA-6 preforms and (b) dual-polymer composites after the post-processing (The areas between two dotted red lines are the samples.)

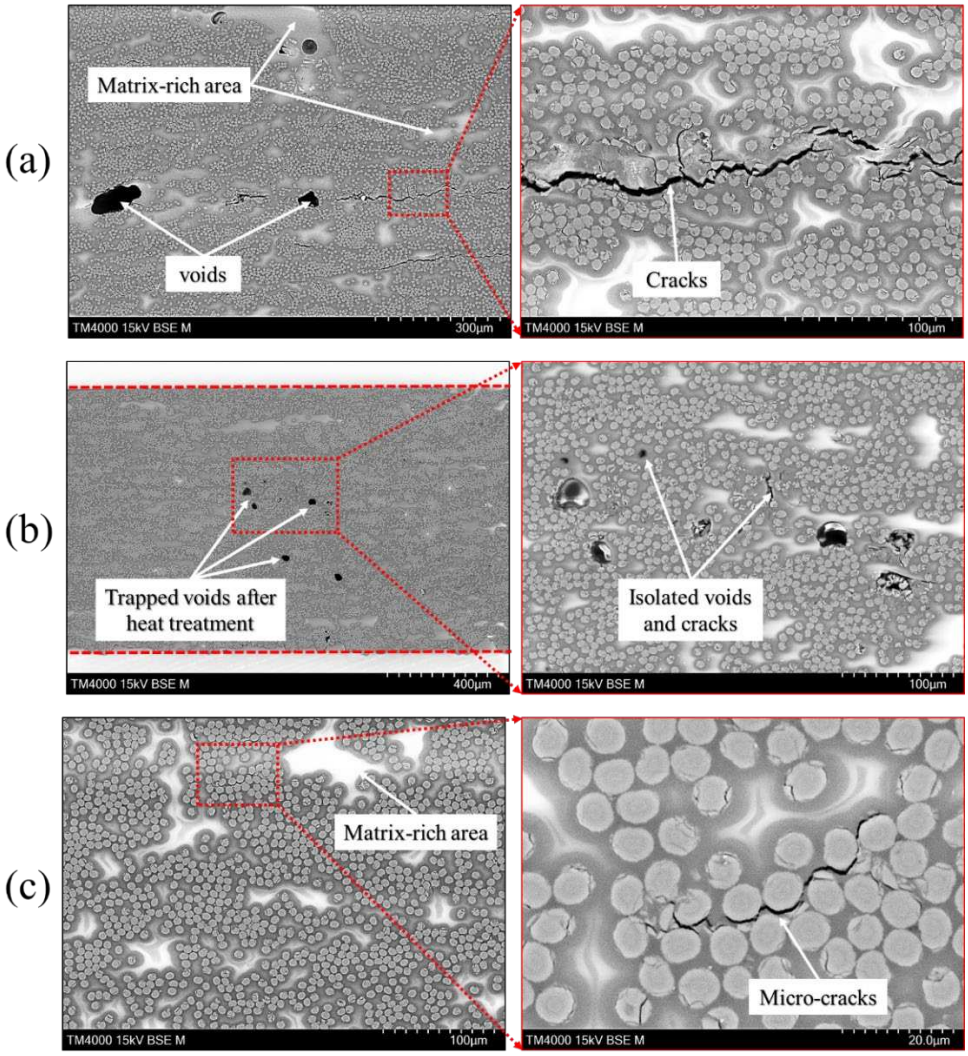

Figure 8. Detailed SEM characterisation for (a) CF/PA-6 preforms before post-processing, (b) CF/PA-6 preforms vacuum-bagged without epoxy powder and (c) dual-polymer composites after the post-processing

4.1.2 Mechanical behaviour

A comparison of the mechanical performance of the UD 0˚ samples are shown in Figure 9. The tensile properties of the samples before post-processing with the powder epoxy are consistent with the result provided from the Markforged material data sheet [42] (strength of 800 MPa and stiffness of 60 GPa). The tensile stiffness and strength of the printed composites could be improved by about 15% with vacuum-bagging only, and they were finally increased by 29.3% and 22.1% (stiffness of 76.9 GPa and strength of 1004 MPa) after post-processing with powder epoxy (according to ASTM D3039 Standard Test Method for Tensile Properties of Polymer

Matrix Composite). The failure strain was slightly decreased due to the brittleness of the added epoxy. The standard deviations were relatively small considering the values of results, as shown in the error bars in the figure.

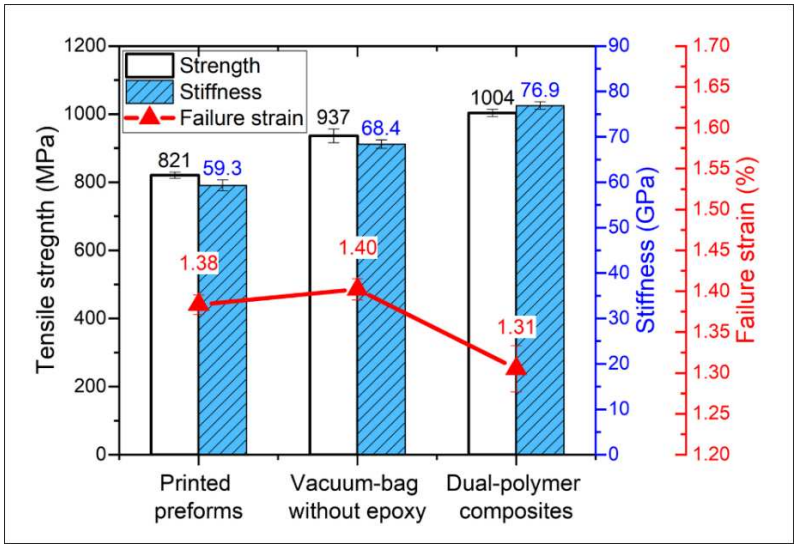

Figure 9. Mechanical performance in the test direction of UD 0˚ CF/PA-6 samples before and after post-processing with/without powder epoxy

Figure 10 shows the comparison between mechanical properties of this study and those from the literature of continuous fibre reinforced composites fabricated by the material-extrusion based printing process [11, 15, 18, 42-53], with the black dashed line indicating the theoretical mechanical property predicted using Rule of Mixtures (RoM) theory [43]. Although all the data points are located below the dashed line, the tensile stiffness and strength after post-processing are just slightly lower (4.2% and 19.9% respectively) than the estimated properties of the CF/PA6 composites from RoM with 34.6 % fibres (80.3 GPa and 1254 MPa, respectively). Meanwhile, some of the values in this study are comparable with the typical aluminium and titanium alloys, which are considered to be the main competitors as they are commonly used in aerospace applications. Only the values from hot-press treatment [15] exhibited both higher tensile stiffness and strength, but the specimens' thickness had a substantial reduction (nearly 50%) due to matrix leakage [15], which was the reason for the large increase of the fibre volume

fraction. As mentioned before, the curved fibre placement cannot be maintained after such treatment, due to the high processing temperature and matrix melting.

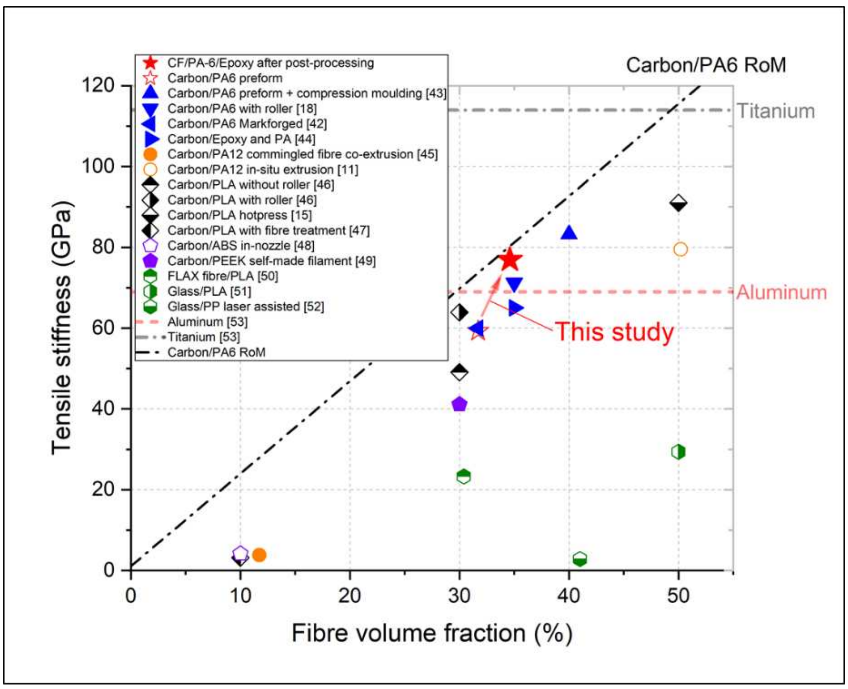

(a)

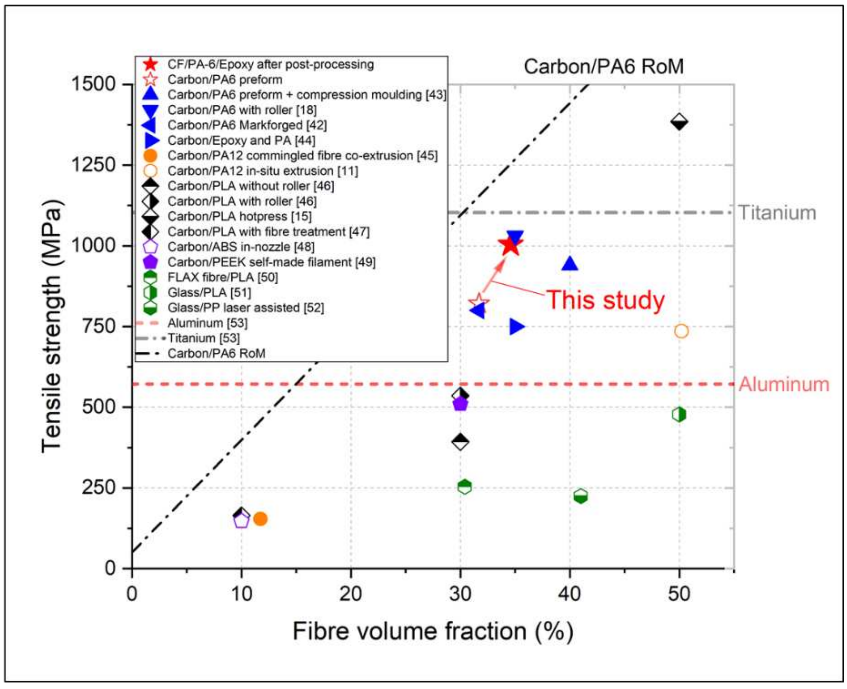

(b)

Figure 10. 3D printed continuous fibre reinforced composites: (a) tensile strength and fibre volume fraction; and (b) tensile stiffness and fibre volume fraction

4.1.3 Fractographic behaviour

Further analysis was conducted by the SEM for the fracture profile, as shown in Figure 11. For the fracture profiles parallel to the fibre direction, it can be seen that the melted epoxy infiltrated the printed composites and infilled the voids between layers, which should effectively reduce the delamination during the loading process. In addition, more fibre breakages were found in the fracture profile of the CF/PA-6 samples after post-processing with epoxy. It meant the treatment with powder epoxy enhanced the bonding between these unidirectional fibre paths and eased the fibre split and crack propagation along the fibre direction.

Figure 11 c & d compares the fracture profiles transverse to the fibre direction. The samples before post-processing exhibited ductile behaviour, in which the voids and cracks led to an inhomogeneous profile with localised stress concentration and then resulted in the yielding of large fibre bundles. Lots of micro-cracks between fibres and matrix were also observed, indicating weak interfacial properties and increased crack propagation. In contrast, the dual-polymer composites after post-processing exhibited a relatively brittle behaviour, with the failure in matrix-rich areas first. Since the adhesion between fibres and matrix was good and no apparent voids occurred in the composites, a homogeneous stress profile was obtained and the sample finally failed with only a few fibres pulled out, resulting from the micro-cracks shown in Figure 8b.

In summary, the melted epoxy infiltrated the CF/PA-6 preforms from the gaps between the print paths and then infilled the apparent voids and interlayer cracks during the curing process. The PA-6 was further consolidated due to the vacuum pressure and its rubbery/viscous state at the melting stage of the curing process. But the epoxy did not get into the micro-cracks/voids between the PA-6 matrix and single carbon fibres, since the PA-6 matrix remained relatively solid to maintain the fibre alignment during the heating cycling.

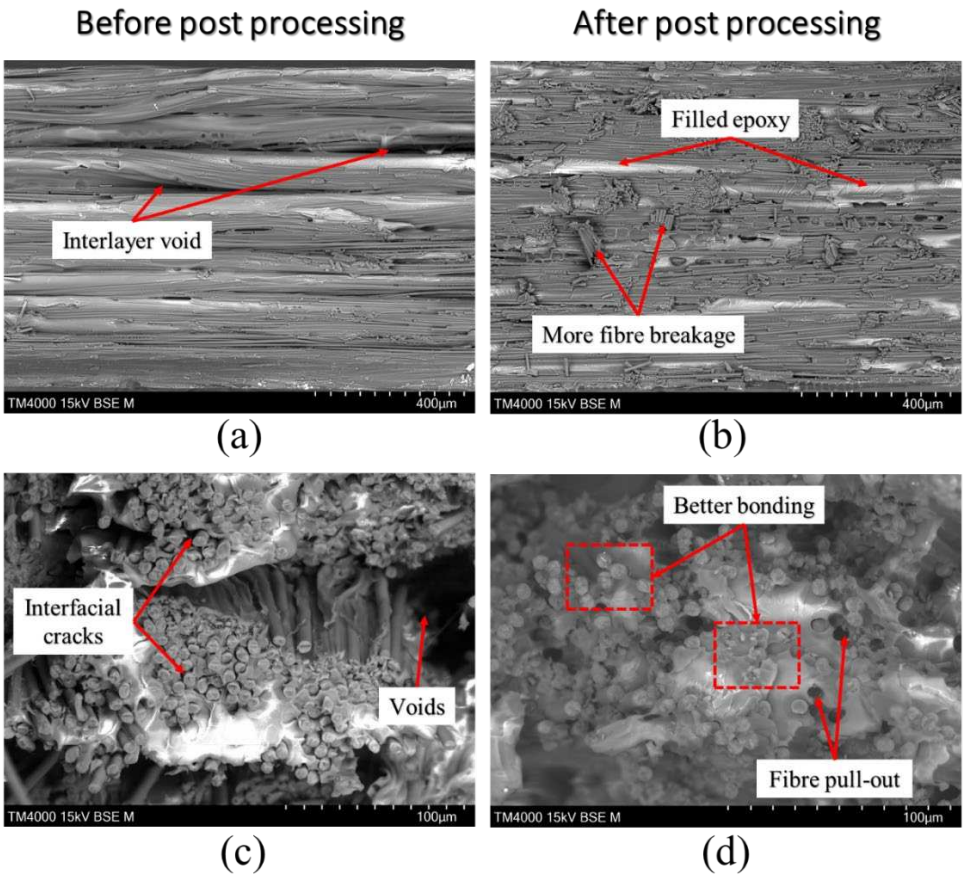

Figure 11. SEM fracture profiles (a) & (b): parallel to; (c) & (d) transverse to the fibre direction

4.2 3D printed single-edge notched plate

The dual-polymer technique allows the manufacturing of composites with low-porosity and customised curved fibre paths. All of the specimens in this section were post-processed via the epoxy-infusion treatment, in order to eliminate the influence of voids and then better investigate the effect of fibre placement. The strength and fracture toughness of three different fibre placement methods for the single-edge notched plate are first presented. The load-displacement curves and the failure pattern are then discussed, also with the distribution of maximum principal strain obtained from the DIC analysis. The ultimate strength is defined as the maximum force carried by the test specimen prior to failure, divided by the gross cross-sectional area (disregarding the notch). The notch stress intensity factor (mode I) K_I at the crack tip under uniaxial stress for the edge crack in a plate is calculated as Eq (1)-(3) [54, 55]:

$$K_I = f(a/w) \cdot \sigma \cdot \sqrt{\pi a} \tag{1}$$

$$f(a/w) = 1.122 - 0.231\left(\frac{a}{w}\right) + 10.55(\frac{a}{w})^2 - 21.71(\frac{a}{w})^3 + 30.382(\frac{a}{w})^4 \tag{2}$$

$$K_{IC} = f(a/w) \cdot \sigma_{peak} \cdot \sqrt{\pi a} \tag{3}$$

where a is the crack length, w is the width of the plate, $f(a/w)$ is the geometry factor and σ is the remote tensile stress. The notch fracture toughness (mode I), K_{IC}, is the highest value of stress intensity that the plate can withstand without fracture [56]. So σ_{peak} is defined as the peak stress without the crack initiation in each case. The data for the calculation of fracture toughness are shown in Table 2.

Table 2. Data of three kinds of single-edge notched samples

	Notch depth a (mm)	a/w	Geometry factor	σ_{peak} (MPa)
Mechanical notched	4.14	0.1118	1.2025	282.49
Concentric infill	3.88	0.1048	1.1924	214.85
Principal stress trajectories	3.52	0.0951	1.1793	888.80

As shown in Figure 12, the strength and fracture toughness of the samples with stress-lines placement were increased by 81.3% and 157.5%, compared to the mechanical notched samples. The improvement of the properties resulted from the stress re-distribution brought from the optimised fibre paths as well as the prevention of the defects caused by the mechanical manufacturing process. As shown in Figure 13, no cracks occurred before the ultimate load of the samples with stress-lines placement. The samples finally failed in a brittle mode, accompanied by symmetrical crack propagation along the angular direction. In contrast, cracks initiated at the tip of the notch during the loading process of the mechanical notched sample. They immediately propagated along the fibre direction when the load came to 58% of the maximum force. The manufactured defect and premature cracks dramatically reduced the fracture toughness of this sample. Subsequent fibre breakage in the transverse direction resulted

in the eventual failure of the sample.

Although no manufactured defeat was introduced to the samples with concentric placement, the strength and fracture toughness were reduced by 31.0% and 33.0% compared to the mechanical notched samples. As shown in Figure 13, cracks initiated near the notch and at the centre of the samples at 60% of the ultimate load, with the former being caused by the stress concentration and the latter resulting from the different mechanical response between the left (curved) and right (straight) parts of the fibres. The final failure exhibited mainly fibre splitting on the left, and only tensile breakage on the right. It revealed that the concentric fibre placement method of composites with complex geometries was inappropriate. The difference between the curved and straight fibres (inevitable in such concentric placement) divided the samples into two parts, which lowered the mechanical properties, even compared with the samples processed by mechanical cutting or drilling. The standard deviations were shown as the error bars in Figure 12, in which the values for those properties depending on the shear failure of the matrix were relatively small, such as the fracture toughness of mechanical notched and concentric infill samples. Larger standard deviations were found for the data that mainly depend on the symmetry of crack propagation. For example, prior to the final fracture of the concentric infill sample, the specimens had already been separated into several parts by the unsymmetrical crack propagation, thus the error of its strength was relatively large. Although consistent trends and failure modes can be seen in this paper, the standard deviations reveal the challenges in predicting crack propagation for composite structures with curved fibre placement.

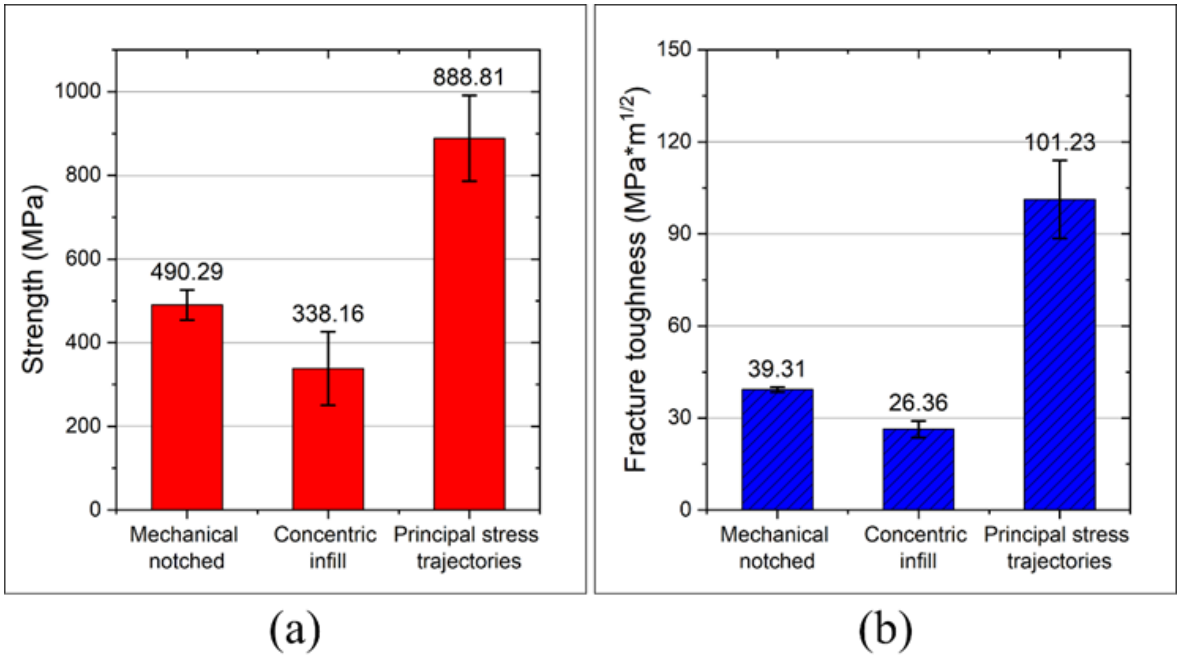

Figure 12. (a) Ultimate strength and (b) fracture toughness of the single-edge notched samples

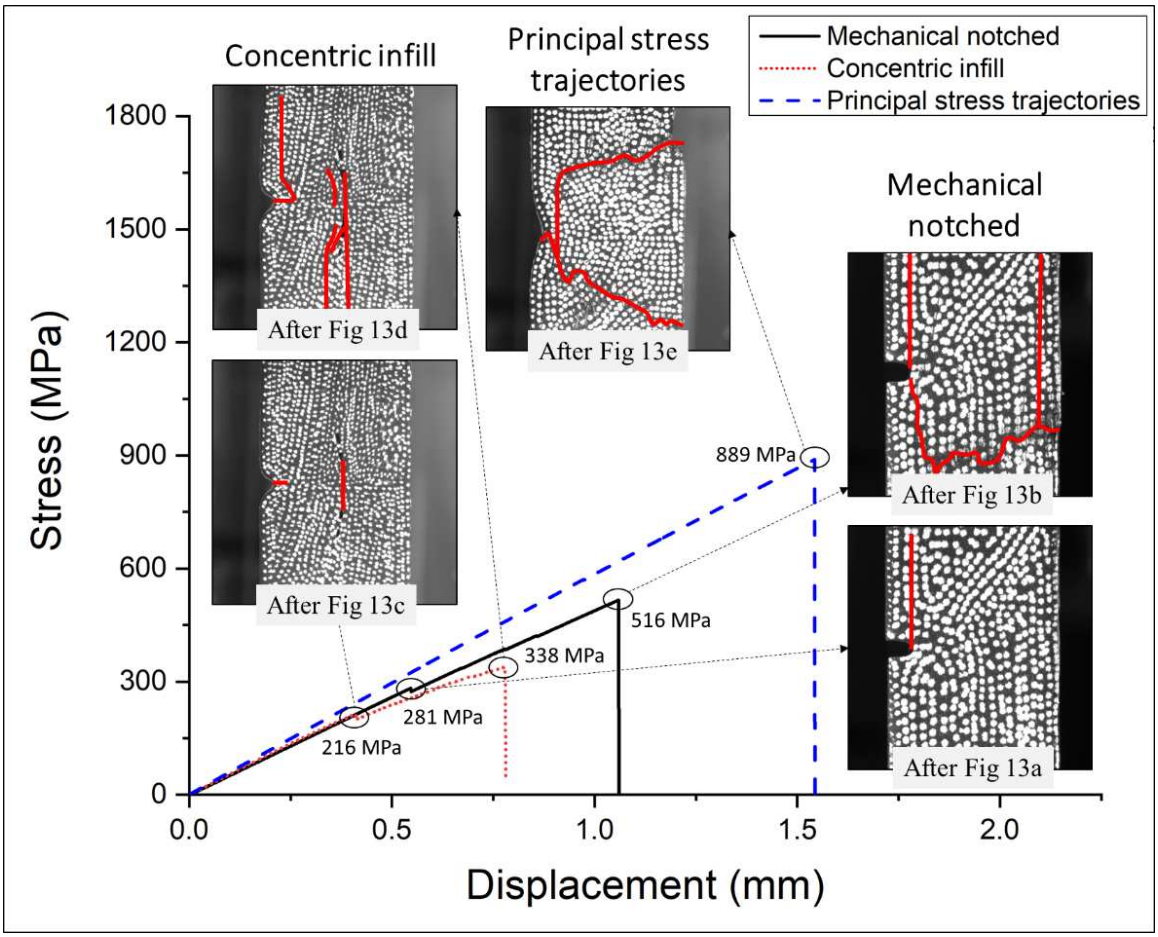

Figure 13. Stress-displacement curves and crack propagation in samples

The distributions of maximum principal strain (prior to failure) are shown in Figure 14, in which (b) & (d) are the states before the ultimate load for the samples with mechanical notched and concentric placement, respectively. A uniform interval type of distribution was adopted for all contour plot legends, in which the contour limit was set as the maximum value of each individual sample to better identify the concentration in the images. Obvious strain concentrations are seen in (b) & (d) due to the cracks, so Figure 14(a) & (c) & (e) are more suitable for evaluating the effect of fibre placement on the stress/strain distribution. For the mechanical notched samples (a) and (b), the highest values of strain are concentrated in a small area around the tip of the notch. For the samples with concentric placement (c) and (d), the highest strain concentrations are also located at the tip of the notch but are extended angularly to the vertical centreline of the samples. Although the manufactured defects were avoided, the semi-circular fibre placement around the notch could not transfer the tensile load properly. For the samples with principal stress-lines placement (e), the strain distribution was quite even and very limited comparatively, since almost the entire domain exhibited in the red colour. It can also be seen that the stress concentration at the tip of the notch was reduced (in the yellow colour, circled) due to the enhancement of the path overlap and the fibre-rich distribution in this area. Compared with the higher values at the area far from the notch (framed), this indicated that the optimised fibre placement method adjusts the material distribution to protect the geometric singularity and prevent the crack initiation. The maximum value of this case was 44.0% lower than that of the concentric case, also 27.3% lower than that of the mechanical notched case. This indicated that the fibre placement along principal stress trajectories distributed the loads from the notch to the whole structure, reducing the localised strain. This improved strain distribution delayed the failure until the applied stress reached 89% of the value required for the fracture of the unnotched specimen (ultimate strength of 1001 MPa for the UD 0° samples).

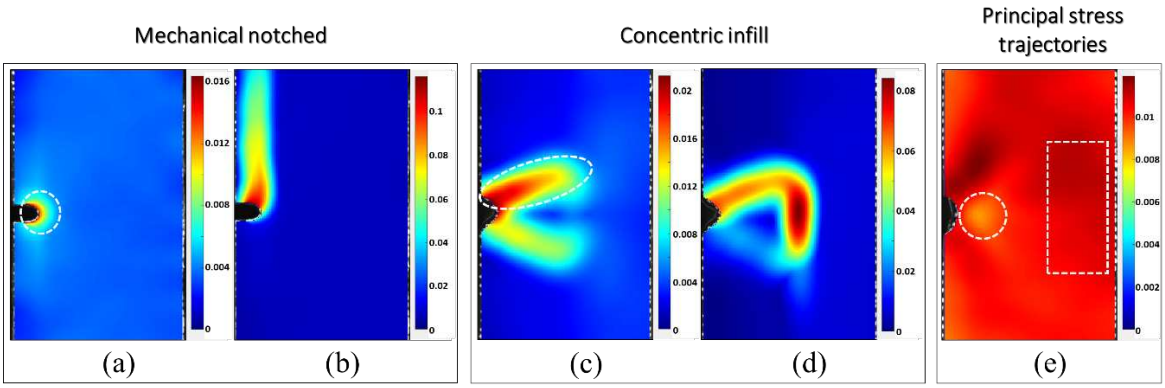

Figure 14. Distribution of maximum principal strain prior to failure: (a) before yielding and (b) ultimate load of the mechanical notched sample; (c) before yielding and (d) ultimate load of the concentric infill sample (e) before failure of the stress-lines sample (different legend scales were used to better identify the strain concentration in each case)

5. Conclusions

In this paper, a low-cost manufacturing technique was presented in which 3D printed thermoplastic composite preforms were infiltrated and cured with a thermosetting powder epoxy, in order to manufacture composites with low-porosity and designed curved fibre paths. The epoxy mainly infiltrated from the gaps between the print paths and dramatically reduced the porosity of dual-polymer composites from 2.69% to 0.06%. The original PA-6 matrix was further consolidated but remained relatively solid to maintain the fibre alignment during the heating and post-processing cycle. DMA and DSC investigations demonstrated that the PA-6 and epoxy polymers are compatible. The tensile stiffness and strength of the carbon fibre reinforced PA-6 composites were improved by 29.3% and 22.1% respectively after the post-processing treatment with epoxy powder. Uniaxial tensile tests of three types of single-edge notched plates were conducted to evaluate the effect of different fibre placement methods. Compared with the mechanical notched samples, optimised fibre placement along the principal stress trajectories increased the strength and fracture toughness by 81.3% and 157.5% respectively. It was also revealed that the general concentric placement method was inappropriate for the material-extrusion based 3D printing of continuous carbon fibre

reinforced thermoplastic composites with complex geometries.

Although the epoxy powders were manually sprinkled onto the printed composites, this epoxy-infusion treatment could potentially be automated in the future by an in-situ powder-sprinkling device, which is integrated with the printer (also with the use of fast-cure epoxy). Also, a special machine for epoxy-infusion could be developed, in which the vacuum bagging (or autoclave) can be automatically set up for the post-processing of parts with complex geometry. Other high-performance thermoplastic composite filaments with high fibre volume fractions could also be used in the future, e.g. carbon fibre reinforced polyether ether ketone, to enable the application of printed composites to meet high-temperature requirements in aerospace and other industrial sectors.

References

[1] Wang X, Jiang M, Zhou Z, Gou J, Hui D. 3D printing of polymer matrix composites: A review and prospective. Composites Part B: Engineering. 2017;110:442-58.

[2] N. Turner B, Strong R, A. Gold S. A review of melt extrusion additive manufacturing processes: I. Process design and modeling. Rapid Prototyping Journal. 2014;20(3):192-204.

[3] Brenken B, Barocio E, Favaloro A, Kunc V, Pipes RB. Fused filament fabrication of fiber-reinforced polymers: A review. Additive Manufacturing. 2018;21:1-16.

[4] Kabir SMF, Mathur K, Seyam A-FM. A critical review on 3D printed continuous fiber-reinforced composites: History, mechanism, materials and properties. Composite Structures. 2020;232.

[5] Dickson AN, Ross K-A, Dowling DP. Additive manufacturing of woven carbon fibre polymer composites. Composite Structures. 2018;206:637-43.

[6] Zhang H, Dickson AN, Sheng Y, McGrail T, Dowling DP, Wang C, et al. Failure analysis of 3D printed woven composite plates with holes under tensile and shear loading. Composites Part B: Engineering. 2020;186.

[7] Zhuo P, Li S, Ashcroft IA, Jones AI. Material extrusion additive manufacturing of continuous fibre reinforced polymer matrix composites: A review and outlook. Composites Part B: Engineering. 2021.

[8] Cheng P, Wang K, Chen X, Wang J, Peng Y, Ahzi S, et al. Interfacial and mechanical properties of continuous ramie fiber reinforced biocomposites fabricated by in-situ impregnated 3D printing. 2021;170:113760.

[9] Uşun A, Gümrük RJAM. The Mechanical Performance of the 3D Printed Composites Produced with Continuous Carbon Fiber Reinforced Filaments Obtained via Melt Impregnation. 2021:102112.

[10] Blok LG, Longana ML, Yu H, Woods BKS. An investigation into 3D printing of

fibre reinforced thermoplastic composites. Additive Manufacturing. 2018;22:176-86.
[11] Liu T, Tian X, Zhang Y, Cao Y, Li D. High-pressure interfacial impregnation by micro-screw in-situ extrusion for 3D printed continuous carbon fiber reinforced nylon composites. Composites Part A: Applied Science and Manufacturing. 2020;130.
[12] Chen Y, Ye L. Topological design for 3D-printing of carbon fibre reinforced composite structural parts. Composites Science and Technology. 2021;204.
[13] Goh GD, Dikshit V, Nagalingam AP, Goh GL, Agarwala S, Sing SL, et al. Characterization of mechanical properties and fracture mode of additively manufactured carbon fiber and glass fiber reinforced thermoplastics. Materials & Design. 2018;137:79-89.
[14] Justo J, Távara L, García-Guzmán L, París F. Characterization of 3D printed long fibre reinforced composites. Composite Structures. 2017.
[15] Yamawaki M, Kouno Y. Fabrication and mechanical characterization of continuous carbon fiber-reinforced thermoplastic using a preform by three-dimensional printing and via hot-press molding. Advanced Composite Materials. 2017:1-11.
[16] Mei H, Ali Z, Yan Y, Ali I, Cheng L. Influence of mixed isotropic fiber angles and hot press on the mechanical properties of 3D printed composites. Additive Manufacturing. 2019;27:150-8.
[17] Li N, Link G, Jelonnek J. 3D microwave printing temperature control of continuous carbon fiber reinforced composites. Composites Science and Technology. 2020;187.
[18] Ueda M, Kishimoto S, Yamawaki M, Matsuzaki R, Todoroki A, Hirano Y, et al. 3D compaction printing of a continuous carbon fiber reinforced thermoplastic. Composites Part A: Applied Science and Manufacturing. 2020;137.
[19] Zhang H, Yang D, Sheng Y. Performance-driven 3D printing of continuous curved carbon fibre reinforced polymer composites: A preliminary numerical study. Composites Part B: Engineering. 2018;151:256-64.
[20] Sugiyama K, Matsuzaki R, Malakhov AV, Polilov AN, Ueda M, Todoroki A, et al. 3D printing of optimized composites with variable fiber volume fraction and stiffness using continuous fiber. Composites Science and Technology. 2020;186.
[21] Hou Z, Tian X, Zhang J, Zheng Z, Zhe L, Li D, et al. Optimization design and 3D printing of curvilinear fiber reinforced variable stiffness composites. Composites Science and Technology. 2021;201.
[22] Nomura T, Kawamoto A, Kondoh T, Dede EM, Lee J, Song Y, et al. Inverse design of structure and fiber orientation by means of topology optimization with tensor field variables. Composites Part B: Engineering. 2019;176.
[23] Li N, Link G, Wang T, Ramopoulos V, Neumaier D, Hofele J, et al. Path-designed 3D printing for topological optimized continuous carbon fibre reinforced composite structures. Composites Part B: Engineering. 2020;182.
[24] Jiang D, Hoglund R, Smith D. Continuous Fiber Angle Topology Optimization for Polymer Composite Deposition Additive Manufacturing Applications. Fibers. 2019;7(2).
[25] Rodriguez JF, Thomas JP, Renaud JE. Characterization of the mesostructure of fused-deposition acrylonitrile-butadiene-styrene materials. Rapid Prototyping Journal. 2000;6(3):175-86.
[26] O'Connor HJ, Dowling DP. Low‐pressure additive manufacturing of continuous fiber‐reinforced polymer composites. Polymer Composites. 2019;40(11):4329-39.
[27] Zhang J, Zhou Z, Zhang F, Tan Y, Tu Y, Yang B. Performance of 3D-Printed Continuous-Carbon-Fiber-Reinforced Plastics with Pressure. Materials (Basel).

2020;13(2).
[28] Pascual-González C, San Martín P, Lizarralde I, Fernández A, León A, Lopes CS, et al. Post-processing effects on microstructure, interlaminar and thermal properties of 3D printed continuous carbon fibre composites. Composites Part B: Engineering. 2021;210.
[29] Robert C, Pecur T, Maguire JM, Lafferty AD, McCarthy ED, Ó Brádaigh CM. A novel powder-epoxy towpregging line for wind and tidal turbine blades. Composites Part B: Engineering. 2020;203.
[30] Chabaud G, Castro M, Denoual C, Le Duigou A. Hygromechanical properties of 3D printed continuous carbon and glass fibre reinforced polyamide composite for outdoor structural applications. Additive Manufacturing. 2019;26:94-105.
[31] Zhang H, Chen J, Yang D. Fibre misalignment and breakage in 3D printing of continuous carbon fibre reinforced thermoplastic composites. Additive Manufacturing. 2021;38.
[32] Maguire JM, Nayak K, Brádaigh CMÓ. Characterisation of epoxy powders for processing thick-section composite structures. Materials & Design. 2018;139:112-21.
[33] Mamalis D, Flanagan T, Brádaigh CMÓ. Effect of fibre straightness and sizing in carbon fibre reinforced powder epoxy composites. Composites Part A: Applied Science and Manufacturing. 2018;110:93-105.
[34] Blaber J, Adair B, Antoniou A. Ncorr: open-source 2D digital image correlation matlab software. Experimental Mechanics. 2015;55(6):1105-22.
[35] Meyer P, Waas AJCPBE. Experimental results on the elevated temperature tensile response of SiC/SiC ceramic matrix notched composites. Composites Part B: Engineering. 2018;143:269-81.
[36] Jo E, Lee S, Hong C, Ji W. In situ observation of interactive failure modes in a single-edge notched symmetric cross-ply laminate using synchrotron X-ray tomography. Composites Part A: Applied Science and Manufacturing. 2020;128:105661.
[37] Nguyen MH, Waas AM. Detailed experimental and numerical investigation of single-edge notched tensile cross-ply laminates. Composite Structures. 2021:114731.
[38] Der Klift FV, Koga Y, Todoroki A, Ueda M, Hirano Y, Matsuzaki R. 3D Printing of Continuous Carbon Fibre Reinforced Thermo-Plastic (CFRTP) Tensile Test Specimens. Open Journal of Composite Materials. 2016;06(01):18-27.
[39] Kim K-W, Kim D-K, Kim B-S, An K-H, Park S-J, Rhee KY, et al. Cure behaviors and mechanical properties of carbon fiber-reinforced nylon6/epoxy blended matrix composites. Composites Part B: Engineering. 2017;112:15-21.
[40] Zhu W, Yan C, Shi Y, Wen S, Liu J, Wei Q, et al. A novel method based on selective laser sintering for preparing high-performance carbon fibres/polyamide12/epoxy ternary composites. Sci Rep. 2016;6:33780.
[41] Mei Z, Chung D. Thermal history of carbon-fiber polymer-matrix composite, evaluated by electrical resistance measurement. Thermochimica acta. 2001;369(1-2):87-93.
[42] Markforged.com. Composites-data-sheet. 2020. p. http://static.markforged.com/downloads/composites-data-sheet.pdf.
[43] He Q, Wang H, Fu K, Ye L. 3D printed continuous CF/PA6 composites: Effect of microscopic voids on mechanical performance. Composites Science and Technology. 2020;191.
[44] Azarov A, Antonov F, Vasil'ev V, Golubev M, Krasovskii D, Razin A, et al. Development of a two-matrix composite material fabricated by 3D printing. Polymer

Science. 2017;10(1):87-90.
[45] Reis Silva M, Pereira AM, Alves N, Mateus G, Mateus A, Malça C. Development of an additive manufacturing system for the deposition of thermoplastics impregnated with carbon fibers. Journal of Manufacturing Materials Processing. 2019;3(2):35.
[46] Omuro R, Ueda M, Matsuzaki R, Todoroki A, Hirano Y. Three-dimensional printing of continuous carbon fiber reinforced thermoplastics by in-nozzle impregnation with compaction roller. 21st International Conference on Composite Materials, Xian, China2017. p. 20-5.
[47] Qiao J, Li Y, Li L. Ultrasound-assisted 3D printing of continuous fiber-reinforced thermoplastic (FRTP) composites. Additive Manufacturing. 2019;30.
[48] Yang C, Tian X, Liu T, Cao Y, Li D. 3D printing for continuous fiber reinforced thermoplastic composites: mechanism and performance. Rapid Prototyping Journal. 2017.
[49] Chen Y, Shan Z, Yang X, Song Y, Zou A. Preparation of CCF/PEEK filaments together with property evaluation for additive manufacturing. Composite Structures. 2021.
[50] Le Duigou A, Barbé A, Guillou E, Castro M. 3D printing of continuous flax fibre reinforced biocomposites for structural applications. Materials Design. 2019;180:107884.
[51] Akhoundi B, Behravesh AH, Bagheri Saed A. Improving mechanical properties of continuous fiber-reinforced thermoplastic composites produced by FDM 3D printer. Journal of Reinforced Plastics Composites and Advanced Materials. 2019;38(3):99-116.
[52] Parandoush P, Tucker L, Zhou C, Lin D. Laser assisted additive manufacturing of continuous fiber reinforced thermoplastic composites. Materials Design. 2017;131:186-95.
[53] Chung D. Carbon fiber composites: Elsevier; 2012.
[54] Liu M, Gan Y, Hanaor DAH, Liu B, Chen C. An improved semi-analytical solution for stress at round-tip notches. Engineering Fracture Mechanics. 2015;149:134-43.
[55] Radaj D. State‐of‐the‐art review on extended stress intensity factor concepts. Fatigue & Fracture of Engineering Materials & Structures. 2014;37(1):1-28.
[56] Kaman MO. Effect of fiber orientation on fracture toughness of laminated composite plates [0° / θ °]s. Engineering Fracture Mechanics. 2011;78(13):2521-34.